# Time-dependent density-functional-theory calculations of the nonlocal electron stopping range for inertial confinement fusion applications

K. A. Nichols [1,2] S. X. Hu [1,2,3,*] A. J. White,[4] V. N. Goncharov,[1,3] D. I. Mihaylov [1] L. A. Collins [4]
N. R. Shaffer,[1] and V. V. Karasiev[1]

[1]*Laboratory for Laser Energetics, University of Rochester, Rochester, New York 14623-1299, USA*
[2]*Department of Physics and Astronomy, University of Rochester, Rochester, New York 14623-1299, USA*
[3]*Department of Mechanical Engineering, University of Rochester, Rochester, New York 14623-1299, USA*
[4]*Los Alamos National Laboratory, Los Alamos, New Mexico 87545, USA*

Nonlocal electron transport is important for understanding laser-target coupling for laser-direct-drive (LDD) inertial confinement fusion (ICF) simulations. Current models for the nonlocal electron mean free path in radiation-hydrodynamic codes are based on plasma-physics models developed decades ago; improvements are needed to accurately predict the electron conduction in LDD simulations of ICF target implosions. We utilized time-dependent density functional theory (TD-DFT) to calculate the electron stopping power (SP) in the so-called conduction-zone plasmas of polystyrene in a wide range of densities and temperatures relevant to LDD. Compared with the modified Lee-More model, the TD-DFT calculations indicated a lower SP and a higher stopping range for nonlocal electrons. We fit these electron SP calculations to obtain a global analytical model for the electron stopping range as a function of plasma conditions and the nonlocal electron kinetic energy. This model was implemented in the one-dimensional radiation-hydrodynamic code LILAC to perform simulations of LDD ICF implosions, which are further compared with simulations by the standard modified Lee-More model. Results from these integrated simulations are discussed in terms of the implications of this TD-DFT-based mean-free-path model to ICF simulations.

## I. INTRODUCTION

Inertial confinement fusion (ICF) research has reached significant milestones in the past few years including achieving a burning plasma state [1,2] and obtaining a target gain $G > 1$ [3] using the indirect-drive scheme. The ICF community suggests that laser direct drive (LDD) is a viable method to obtain a high gain with inexpensive targets. In the LDD scheme of ICF, target acceleration relies on the thermal conduction of electrons which absorb laser energy in coronal plasmas and then transfer these energies to the ablation front of the target. The plasma region between the location of critical electron density and the ablation front is called the *conduction zone* in LDD. Nonlocal electrons ($E_k = 10 - 20$ keV) heated by intense laser light in the coronal plasmas will transverse the conduction zone to provide the ablation pressure for ICF target implosions. Understanding how these nonlocal electrons lose energy in the conduction-zone plasma is crucial for understanding laser-target coupling in LDD ICF modeling [4]. In LDD, a typical ICF target consists of deuterium-tritium (DT) gas, enclosed by a solid mixture of DT, and encapsulated by a thin ablative shell of polystyrene (CH). As intense laser beams illuminate the ICF target, the CH layer is heated and ablated; shocks are launched to compress the DT layer; the continuous

laser ablation accelerates the target to implode up to a high velocity of $v_{imp} > 3.7 \times 10^7$ cm/s [5].

During this laser-ablation process, the laser energy is absorbed in the coronal plasma below the critical surface and carried to the ablation front in the form of high-energy electrons; the critical surface is the radius that coincides with the critical electron density (in CH, this corresponds to a mass density $\rho_C \approx 0.04$ g/cm$^3$) [6]. As these energetic and nonlocal electrons move through the conduction zone, they interact with and lose energy to the background CH and DT plasmas. In some cases, the electrons reach thermal equilibrium with CH or DT. In this paper, we define the stopping range or mean free path (MFP) of a nonlocal (projectile) electron as the distance it travels before its velocity drops to the electron thermal velocity of the background plasma. Thus, understanding and calculating the nonlocal electron MFP is crucial for accurate simulations of ICF experiments and understanding laser-target energy coupling.

Over the past few decades, different models based on traditional plasma physics have been developed to model the nonlocal thermal transport for high-energy-density (HED) plasmas [7–10]. For instance, the current model for nonlocal electron thermal conduction in the one-dimensional (1D) radiation-hydrodynamic code LILAC [11] is a modified version of the Lee-More method [10,12]. As shown in Ref. [12], the conduction model inaccurately predicts the optical depth modulation, among other quantities, compared with experimental results performed on OMEGA. More recently,

*Corresponding author: shu@lle.rochester.edu

experimental evidence has also indicated that the CH-DT interface retreats differently between experiments and LILAC simulations [13,14]. These observations have motivated us to seek a more accurate model of the nonlocal electron MFP to improve the predicative capability of LDD implosion simulations.

Stopping power $(SP) = -dE/dx$ is directly related to the nonlocal electron stopping range; the nonlocal electron is treated as the projectile stopping in a given material [12]. There are many analytical formulas that model the SP of ions in classical and quantum materials including the Li-Petrasso (LP) method [15], the Brown-Preston-Singleton (BPS) method [16,17], and the dielectric function (DF) formalism [18]. These models, although computationally inexpensive, are established by the homogeneous electron gas and generally neglect any partial ionization effects. They also fail to incorporate phenomena including the Barkas effect [19,20] and $Z_1$ oscillation [21]. The former accounts for the fact that SP is dependent on the sign of the projectile charge, meaning under the same conditions, a proton and an antiproton would exhibit distinct SPs [19,20]. The latter accounts for the oscillations of the SP due to the projectile charge [21]. Thus, we turn to *ab initio* methods such as the time-dependent density functional theory (TD-DFT), including the orbital-free (OF) and stochastic Kohn-Sham (KS) schemes, to calculate the nonlocal electron SP and MFP.

In this paper, we will outline the TD-OF-DFT algorithm [22], in Sec. II, accompanied by a brief discussion of the time-dependent stochastic DFT (TD-sDFT). In Sec. III, we present the SP and MFP results from direct TD-DFT calculations of nonlocal electron stopping in conduction-zone CH plasmas relevant to LDD ICF. We then fit these TD-DFT results to obtain our global, analytical model with numerical coefficients for the nonlocal electron MFP. These results are compared with other SP models as well as the modified Lee-More model currently used in LILAC [12]. In Sec. IV, we implement this global and TD-DFT-based MFP model into LILAC and demonstrate its effect on LDD implosions through LILAC simulations. The simulation results are also discussed. Finally, we summarize these findings in Sec. V and include additional discussions and plans for improvement.

## II. METHODOLOGY

### A. TD-DFT

The first-principles TD-DFT has been applied to perform calculations for different dynamic properties of plasmas [23–26]. Thus, TD-DFT has been used to reproduce and obtain SP results in warm dense matter [27–31]. Our SP calculations are performed using the OF approach to TD-DFT [32]. While the Mermin-KS (MKS) approach to DFT [33,34] is more accurate than the OF method, the MKS method has computational costs that scale cubically with volume and temperature [28,33]. Moreover, the temperature regime we consider for an ICF polystyrene plasma (100–1000 eV) is extreme enough that the OF treatment becomes reasonably accurate [22]. Thus, for the sake of computational resources and time, we mostly utilized TD-OF-DFT for our simulations. We benchmarked some of our calculations using TD-sDFT.

Overall, our TD-DFT results of nonlocal electron SP (and stopping range) are obtained using the recently developed stochastic and hybrid representation electronic structure by DFT (SHRED) code [19].

The OF method for DFT follows a similar approach to the KS approach to DFT. However, in the OF-DFT method, the electron density $\rho(\mathbf{r})$ is represented using a single, collective orbital $|\psi(\mathbf{r})|^2 = \rho(\mathbf{r})$, while in the MKS approach, the density is defined as a sum of many noninteracting orbitals $\rho(\mathbf{r}) = \sum_n f_n \psi_n^*(\mathbf{r})\psi_n(\mathbf{r})$ for Fermi-Dirac occupations $f_n$. We can extend this OF approach to include time-dependent effects by defining the orbital using the scalar velocity field $\nabla S(\mathbf{r},t)$ such that $\psi(r,t) = \sqrt{\rho(\mathbf{r})} \cdot \exp[iS(\mathbf{r},t)]$; we write the time-dependent version of the single particle Schrodinger-like equation as [22,30]

$$i\frac{\partial \psi(\mathbf{r},t)}{\partial t} = \left[\frac{-\nabla^2}{2} + \hat{V}_{\text{eff}}(\mathbf{r},t)\right]\psi(\mathbf{r},t). \quad (1)$$

In the above equation, the effective potential [for $\rho = \rho(\mathbf{r},t)$] is defined as

$$\hat{V}_{\text{eff}}(\mathbf{r},t) = V_H(\rho,\mathbf{r}) + \frac{\delta F_{\text{s-vW}}^{\text{TF}}[\rho]}{\delta\rho} + \frac{\delta E_{\text{xc}}[\rho]}{\delta\rho} + V_{\text{ext}}, \quad (2)$$

and is the sum of the contributions from the mean-field Hartree potential $V_{\text{H}}(\rho,\mathbf{r})$, the Thomas-Fermi plus von Weizsäcker noninteracting free energy $\frac{\delta F_{s-vW}^{\text{TF}}[\rho, T]}{\delta\rho}$ [35,36], the exchange correlation potential $\frac{\delta E_{\text{xc}}[\rho]}{\delta\rho}$, and the external potential $V_{\text{ext}}$, for electron-ion interactions. Equations (1) and (2) give the typical TD-OF-DFT algorithm, which is called Thomas–Fermi–von Weizsäcker approach to TD-DFT. To better catch the time-dependent response, however, we include the addition of current-dependent energy density potential $V_{\text{CD}}(\mathbf{r},t)$ based on the Lindhard response and defined in Ref. [22], to the overall effective potential $\hat{V}_{\text{eff}}$. As discussed in Ref. [22], the addition of this term is shown to improve the SP calculations near the Bragg peak; moreover, including this dynamic term creates a nonadiabatic version of TD-OF-DFT [22,30].

In addition to the TD-OF-DFT method used for most MFP calculations for nonlocal electrons in conduction-zone CH plasmas, we have also applied TD-sDFT to benchmark some of our TD-OF-DFT calculations. The details about the TD-sDFT method have been given in a recent paper, see Refs. [28,37]. Here, we briefly outline the basics. TD-sDFT calculations [28,38–40] are an extension of the typical MKS method; this method enables high-temperature calculations viable for $T \gg T_{\text{F}}$ (with $T_{\text{F}}$ being the Fermi temperature for a given electron density). TD-sDFT, as described extensively in Refs. [28,38,39], uses the Hutchison method to estimate the initial electron density using stochastic Rademacher vectors [40]. When converged, TD-sDFT reaches the same accuracy as the typical KS approach, but as it scales linearly with size and inversely with temperature, it costs much less computationally for the HED systems described in this paper.

### B. TD-DFT calculations for nonlocal electron SP

We use the above TD-DFT algorithm to set up our SP simulations in polystyrene. Equations (1) and (2) are

self-consistently solved for both the incoming electron and the background CH plasma using the split operator method [41]. For our simulations, we take a single, high-energy electron with different kinetic energies up to 25 keV and project it along the $z$ axis into a box of CH plasmas with a given temperature and mass density. To account for relativistic effects, we use the Einstein relation for kinetic energy $K = [(pc)^2 + (mc^2)^2]^{1/2} - mc^2$ to determine the corresponding input velocity from the momentum $p = \gamma v m$, with $\gamma$ being the Lorentz factor.

For each density-temperature condition, we perform convergence tests for the time step, grid size, and box size. For the sake of computational and time resources, we have converged our TD-DFT calculations to $\sim 10\%$ accuracy. Our simulations are run for boxes between 256 and 320 atoms and a ratio of [1:1:(4–5)] for the simulation box lengths of $L_x$, $L_y$, and $L_z$. Thus, the length of the box along the direction of motion ($z$) ranges from 44.22 to 96.03 Å. The time step for TD-DFT calculations is $3 \times 10^{-3}$ atomic units $\cong 7.26 \times 10^{-5}$ fs. Moreover, the grid points in the $x$ direction are between 128 and 320. The grid spacing is directly related to the energy cutoff [28], which defines the max energy of the plane-wave basis.

We have used the Perdew-Burke-Ernzerhof exchange-correlation functionals [42] implemented through the LIBXC package [43]. For our calculations, pseudopotentials are used; for carbon, we use an all-electron Hartwigsen-Goedeker-Hutter (HGH) pseudopotential, and for hydrogen, we utilize the Goedecker pseudopotential [44–47]. Furthermore, for the electron projectile, we utilize the same pseudopotential as the hydrogen (proton); however, we take the charge to be $-1$ and, in our simulation, set the mass to be the electron mass. Thus, the incoming electron is treated as a classical particle with a negative charge and mass of an electron, while the background electrons are treated quantum mechanically. The approximation that the electron projectile is treated classically in our current TD-DFT calculations should be reasonable, as nonlocal thermal transport is mainly concerned with energetic electrons ($\sim 6$ kT), which are significantly more energetic than the background plasma electrons ($\sim 1$ kT).

We have used OF-DFT molecular dynamics (OFMD) simulation to generate different configurations of the background CH plasma. Namely, for a given mass density, plasma temperature, and box size, the C and H atoms are randomly positioned into the simulation box; finite-temperature DFT calculations determine the mean-field electron density for a given ionic configuration, from which the Hellman-Feynman theorem will tell us the electronic force acting on each ion. Combining the electronic force with the ionic forces, the total force will move each ion to its new location for a given time step by classical Newton's equation. Such a molecular dynamics (MD) process is repeated thousands of time steps to sample different configurations of the background CH plasma. This *ab initio* DFT-MD method [48–50] has extensively been used to simulate plasmas ranging from warm dense matter to ideal plasmas in the past two decades. For the results presented here, the CH plasma density varies from 0.05 to $1.0\,\text{g/cm}^3$ and temperature ranges from 100 to 1000 eV, corresponding to plasma types varying from partially ionized nonideal ones

to ideal plasmas. As shown in Fig. 1, since OFMD simulations go beyond the homogeneous electron gas, we see slight fluctuations in the electron density. With the OFMD-generated configurations, we take evenly spaced time snapshots of the background plasma for TD-DFT calculations through which the nonlocal electrons propagate. For each TD-DFT simulation, the positions of the ions are held constant because the time of projectile passing through the plasma is short ($\sim 1$ fs). The SP is then computed using TD-DFT as the average TD mean-field force on the electron projectile at a given time using the Hellman-Feynman theorem [22,28] such that $\frac{dE}{ds} = \langle F_{\text{proj}}(\rho, \mathbf{R}, t) \rangle$, where the vector $\mathbf{R}$ is the position of the projectile computed using classical equations of motion. The full force equation is given in Refs. [22,28].

Moreover, the average force on the projectile is directly related to the SP defined in this paper as

$$-\frac{dE}{dz} = -\frac{dE}{ds} \cos(\theta_D), \tag{3}$$

where $\theta_D$ is the electron angle of deflection (discussed below) and $dE/ds$ is defined above. There are two ways to compute the SP in TD-DFT calculations: one where the projectile is propagated through the plasma at a constant velocity and the other where the projectile can change velocity as it propagates causing deflection/scattering to occur. For heavy ion projectiles, both methods will give similar results as the deflection effect is negligible. However, for a light electron projectile, we must incorporate this deflection angle. To obtain $dE/ds$, we run the above simulation with the projectile momentum fixed solely in the $z$ direction. We then run a second simulation to allow the electron to scatter to obtain the deflection angle $\theta_D$, discussed below. Combining these two results, we obtain our SP given in Eq. (1). To improve our statistics, we allow the electron projectile to pass through the $z$ direction of the box multiple times (10 passes); starting at the time it takes for the electron to reach $L_z/8$, we continuously calculate the rolling average force $\langle \frac{dE}{ds} \rangle$ on the electron. After the simulation has ended, we take the mean of the rolling average measurements as the value $\frac{dE}{ds}$ for the given conditions; we exclude the rolling average measurements from the first two passes (up to $2L_z$) in our second average to avoid extremes caused by the initial oscillatory behavior of the SP. For most results presented here, we have averaged over at least two snapshots of the background CH plasma. Because the conduction-zone plasmas are approaching a weakly coupled case, we find that different snapshots yield very similar SP results.

To give an example of these TD-DFT calculations, Fig. 1 shows time snapshots of the difference between the instantaneous and initial electron density in the $y - z$ plane for a single electron stopping in CH at $0.50\,\text{g/cm}^3$, 500 eV. In this figure, we allow the electron to change velocity as it moves through the plasma. The white dotted line shows the undeflected path of the electron; each box contains 320 atoms with a 1:1:5 ratio between $L_x$, $L_y$, and $L_z$. Figures 1(a)–1(c) show time snapshots for an electron projectile with 6 keV initial kinetic energy; Figs. 1(d)–1(f) are time snapshots for an electron with an initial kinetic energy of 20 keV. For every run, the electron projectile starts from the location $(L_x/2, L_y/2, 0)$. We see the trajectory of the nonlocal electron as it propagates along the $z$ axis and interacts with the background CH plasma.
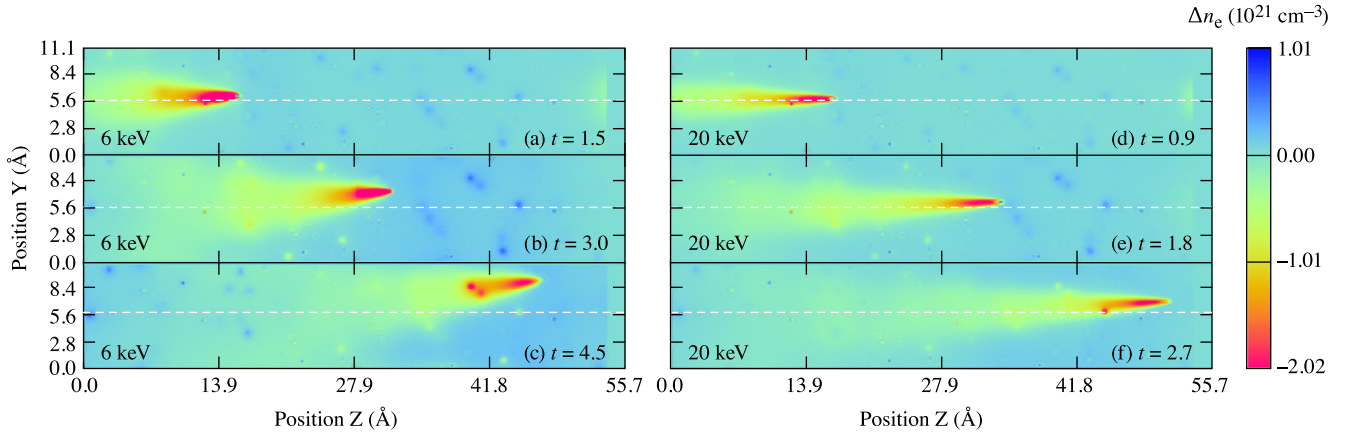
FIG. 1. Two-dimensional snapshot in the $y - z$ plane of the difference between the instantaneous and initial electron density $\Delta n_e$ (1/cm$^3$) for a single electron stopping in CH at 0.50 g/cm$^3$, 500 eV. The panels show the trajectory of the electron as it progresses through the CH and is scattered. (a)–(c) show time snapshots for an electron projectile with 6 keV initial kinetic energy. (d)–(f) are time snapshots for an electron with an initial kinetic energy of 20 keV. The lengths of the simulation box are given in angstroms.

The projectile electron leaves a clear wake as it progresses through the CH plasma. This kind of plasmonic behavior, as discussed in Ref. [51], induces a drag force on the projectile due to dynamic response that contributes to the overall SP and is included in our TD-DFT calculations. Furthermore, as the incoming electron moves along the $z$ direction of the box, it is scattered in the $x$ and $y$ directions. This deflection is apparent for low-velocity projections [see Figs. 1(a)–1(c)], but when the electron projectile velocity is much larger than the thermal velocity of the background electrons ($v_{\mathrm{proj}} \gg v_{\mathrm{th}}$), the deflection is less significant to the overall stopping [see Figs. 1(d)–1(f)]. For all incoming electrons, we calculate this angle of deflection $\theta_D$ such that $\cos(\theta_D) = \frac{\Delta z}{\sqrt{\Delta x^2 + \Delta y^2 + \Delta z^2}}$, where $\Delta x$, $\Delta y$, and $\Delta z$ are the distances the electron projectile has moved from its initial point. To calculate this deflection angle for a given set of plasma conditions, we run the same simulation as discussed above; however, we allow the electron to accelerate/decelerate as it travels through the polystyrene. We look at the trajectory of the electron, to calculate the angle of deflection. Like our calculations of $dE/ds$, we take the rolling average of $\cos(\theta_D)$; however, we only calculate $\theta_D$ until either the electron is deflected past the length of $L_x$ or $L_y$ or until one complete pass in the $z$ direction. Again, we take the mean of the rolling average values as the final value of $\theta_D$. Different from the $dE/ds$ measurements, we generate $\theta_D$ using only one ionic configuration for each set of distinct ($\rho$, $T$, $K$). Finally, using our obtained values for $\theta_D$ and $dE/ds$, we calculate the SP defined in Eq. (3).

### C. Modified Lee-More model for the MFP of nonlocal electrons

To investigate the implications of our TD-DFT results to LDD implosion simulations, we discuss the current nonlocal electron conduction model used in radiation-hydrodynamic codes for ICF target design and simulations in this subsection. A modified version of the Lee-More model [10,12] has been used to calculate the nonlocal electron transport in the 1D hydrocode LILAC; the general algorithm for this previously established method is discussed below. Moreover, we note

that, by fully examining the formulation, the velocity scaling of the collective CL can properly approach the classical Bohr ($\sim v^3$) or the quantum Bethe ($\sim v^2$) limit [52,53]. With this model, the general electron penetration depth is given as [12]

$$\lambda_E = \sqrt{\lambda_K \lambda_{90}}, \tag{4}$$

where

$$\lambda_k = \frac{K^2}{4\pi e^4 (n_e^T \Lambda_e + n_e^f \Lambda_c)}, \tag{5}$$

$$\lambda_{90} = \frac{K^2}{2\pi e^4 (\Lambda_e + Z \Lambda_i / 2)} \tag{6}$$

are the electron deposition path and 90° scattering path defined as a function of the nonlocal (projectile) electron kinetic energy $K$, the total and free-electron densities ($n_e^T$, $n_e^f$), and the specified CL. The electron-ion and electron-electron CLs are defined as

$$\Lambda = \ln\left(\frac{b_{\max}}{b_{\min}}\right), \tag{7}$$

using the maximum $b_{\max}$ and minimum $b_{\min}$ impact parameters for Coulomb scattering such that

$$b_{\max} = \max[\lambda_D, (3/4\pi n_i)^{1/3}], \tag{8}$$

$$b_{\min}^i = \max\left(\frac{\hbar}{m_e v}, \frac{\langle Z \rangle e^2}{2K}\right),$$

$$b_{\min}^e = \max\left(\frac{\hbar}{m_e c}\sqrt{\frac{2}{\gamma - 1}}, \frac{e^2}{2K}\right). \tag{9}$$

Above, $\lambda_D$ is the Debye length, $n_i$ is the ion density, and $\gamma$ is the Lorentz factor. Each of the above parameters reflects a physical limit; $b_{\max}$ is determined by either the Debye length or the average ion radius to account for screening. The parameter $b_{\min}$ is defined as a function of the particle energy; at low energy, it is the minimum impact parameter by a classical electron, while at high energy, it is the minimum distance constrained by the uncertainty principle [10,12]. Furthermore,

the CL due to collective effects is defined as

$$\Lambda_c = \ln\left(\frac{1.123v}{\omega_p b_{max}}\right), \tag{10}$$

for plasma frequency $\omega_p$ and projectile velocity $v$. For highly ionized plasmas, this effectively replaces $b_{max}$ with a velocity-dependent cutoff.

The original Lee-More method is based upon the kinetic Boltzmann equations and neglects electron-electron scattering; thus, the algorithm becomes inaccurate for low-$Z$ materials; however, the modified version, although still based on the Boltzmann equations, has been updated to include electron-electron collisions, as shown in Eqs. (4)–(6) [10]. This method, while computationally simple, does not accurately predict the MFP of nonlocal electrons, as evidenced by experimental soft x-ray self-emission images in cryogenic DT implosions on OMEGA [14]. Our *ab initio* TD-DFT calculations are intended to examine if there is any deviation from the modified Lee-More model for nonlocal electrons traversing the conduction-zone CH plasmas in LDD implosions.

## III. RESULTS

### A. Electron SP in conduction-zone polystyrene plasmas

Using the above TD-OF-DFT methodology, we obtain SP results for a high-energy electron traversing the CH plasma for ICF conditions. Prior to developing our global model for the MFP, we looked directly at our SP data obtained from TD-OF-DFT calculations. We probed seven unique density-temperature conditions of CH plasmas at mass densities of $0.05-1.0\,\text{g/cm}^3$ and temperatures of 100–1000 eV, with nonlocal electron (projectile) kinetic energy values up to 25 keV. These unique plasma conditions span the necessary conduction-zone regime. Since TD-DFT calculations are computationally expensive, we computed $(-dE/ds)$ for 10–12 distinct nonlocal electron kinetic energy values for each unique plasma condition. Figure 2 shows the SP $(-dE/dz)$ distributions for each of these plasma conditions. The individual points represent the exact TD-OF-DFT calculations with the deflection angle considered; the corresponding curves are the individualized fits. Each of the points in Fig. 2 corresponds to the SP averaged over two snapshots, meaning that, for each projectile kinetic energy value, we have repeated the TD-OF-DFT calculations with two different configurations of the background CH plasma. The two-snapshot calculations generally resulted in distinct but similar SP results. Here, we interpolate/fit each set of data using the sum of multiple ($i$) weighted Gaussian distributions: $SP = \sum_i a_i \exp[-(K-b_i)^2/2c_i^2]$ with numerically determined coefficients $(a_i, b_i, c_i)$ to interpolate the data. Such a fitting serves solely as an interpolation of each TD-DFT dataset, which enables the numerical integration for calculating the MFP of nonlocal electrons. The small inaccuracy near the high-energy endpoint would not significantly affect the MFP calculations, shown by the integration in Eq. (11).

Moreover, in Fig. 3, we compare our TD-DFT results for a CH plasma at $0.50\,\text{g/cm}^3$, 500 eV to the BPS [16,17], LP [15], and DF [18] methods for SP. We note that, while the three analytical models assume a uniform electron density, the TD-DFT results, as shown in Fig. 3, allow for fluctuations in the
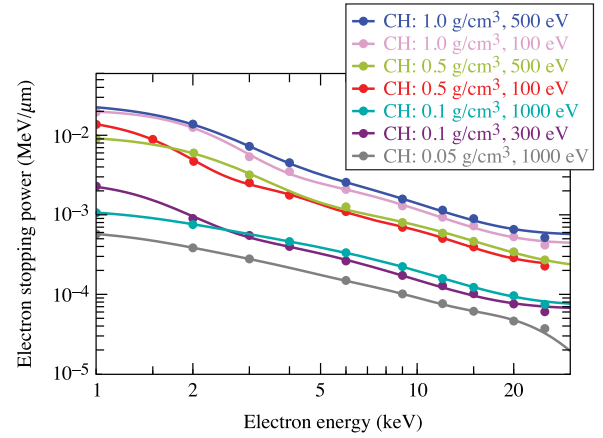


FIG. 2. Electron stopping power (SP) $-dE/dz$, for a high-energy electron stopped in CH plasma as a function of initial electron kinetic energy. The individual points are the TD-OF-DFT calculations; the corresponding curves are the individual fits. The plasma conditions assessed are between 0.05 to $1.0\,\text{g/cm}^3$ and 100 to 1000 eV, conditions relevant to inertial confinement fusion (ICF) conduction-zone plasmas.

electron density along the trajectory of the electron. Overall, we see that, for the highly energetic electrons, TD-DFT predicts considerably smaller SP than all three analytical models by a factor of $\sim 2$. We note that previous results of ion stopping in warm dense matter showed that TD-DFT exhibited lower SP by $\sim 15-25\%$ compared with traditional plasma models [22,27,30]. Furthermore, previous experimental results on proton stopping [29,30,31] showed that TD-DFT calculations (in both the KS and OF formulation) not only aligned well with experimental data but outperformed analytical models including BPS, LP, and DF.

To understand what causes this lower SP, we have explored the background electron density along the projectile trajec-
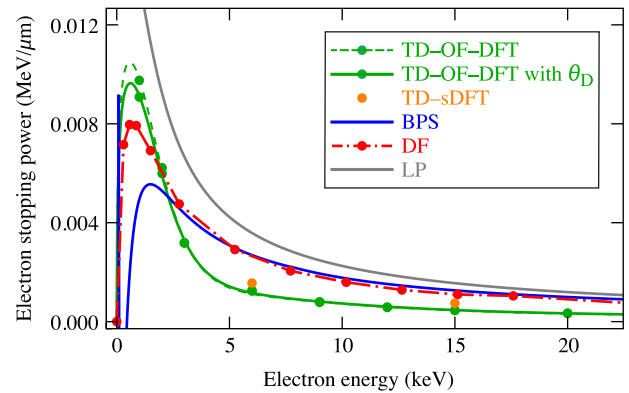


FIG. 3. Electron stopping power (SP) in $0.50\,\text{g/cm}^3$, 500 eV CH plasma, with a comparison between the Brown-Preston-Singleton (BPS; blue), dielectric function (DF; red), and Li-Petrasso (LP; gray) analytical models for SP and our time-dependent density functional theory (TD-DFT) data. The solid green curve represents the TD-DFT data with the deflection angle $\theta_D$ considered, while the dashed green curve is the TD-DFT data without deflection/scattering considered.

tory in TD-OF-DFT simulations. The resulting distribution, however, averaged out to the uniform electron density assumed by the usual plasma models. The Barkas effect can partially explain the large discrepancy between TD-DFT calculations and analytical models. The Barkas effect considers that a negatively charged projectile has a lower SP than a positively charged projectile of the same mass. Traditional plasma models for SP typically assume the projectile is positively charged or that the sign of the projectile charge does not matter if the first Born approximation is invoked; however, TD-DFT goes beyond this assumption [19,20,54]. To quantify this effect, we performed TD-OF-DFT calculations for a high-energy positron moving in a CH plasma of $0.50 \, \text{g/cm}^3$ and 500 eV temperature. We tested the positron projectile energies of 2, 6, and 12 keV. The results showed, compared with the electron projectile case, the positron exhibited a $\sim 17 - 42\%$ relative increase in SP. Thus, this Barkas effect can partially explain the lower SP using TD-DFT calculations compared with the traditional plasma models.

Finally, in Fig. 3, we benchmark our SP results to TD-sDFT [28,38–40], briefly described above and fully derived in Ref. [28]. For our TD-sDFT calculations, shown in orange, we use 200 stochastic orbitals and keep all remaining parameters (time step, box size, ion configuration, etc.) the same as our TD-OF-DFT calculations. For the sake of computational resources, we only validate a few points. Again, we take the rolling average SP with respect to time, starting at the time for the electron to progress to $L_z/8$. We take the average of the rolling average SP, beginning at the time it takes the electron to progress to $3L_z$, then remove the first three passes to minimize the contribution of the initial stochastic fluctuations to the overall stopping. For the stochastic points, we allow the electron to accelerate/decelerate while it progresses through the plasma and take the SP shown in Eq. (3), where $\theta_D$ is the same angle determined by the TD-DFT calculations. Figure 3 indicates that the stochastic results align well with the TD-OF-DFT results, indicating that the TD-OF-DFT algorithm is in fact valid in this extreme temperature regime (degeneracy parameter: $\theta \gg 1$, $T \geqslant 100 \, \text{eV}$).

### B. Nonlocal electron MFP

We utilize our generalized SP data to derive a global model for the nonlocal electron deposition path (range) based on our plasma parameters and initial nonlocal electron kinetic energy. The SP calculations are directly related to the MFP $\lambda_E$ using the integral:

$$\lambda_E = \int_{\frac{3}{2}k_b T}^{E_0} \frac{dE}{-dE/dz}, \quad (11)$$

where $E_0$ is the initial kinetic energy of the electron, $T$ is the temperature of the background plasma, and $-dE/dz$ is our SP. We denote the MFP as the distance before the nonlocal electron loses enough energy to the plasma that it reaches thermal equilibrium [$E_0 < (3/2)k_b T$] with the background electrons. Thus, the low-energy limit for integration in Eq. (11) is taken to be $(\frac{3}{2})k_b T$ rather than zero. Moreover, we take the MFP to be zero for any nonlocal electrons with [$E_0 < (\frac{3}{2})k_b T$]. Using this integral and our interpolated SP data, we obtain MFP data for all the CH plasma densities and temperatures examined.
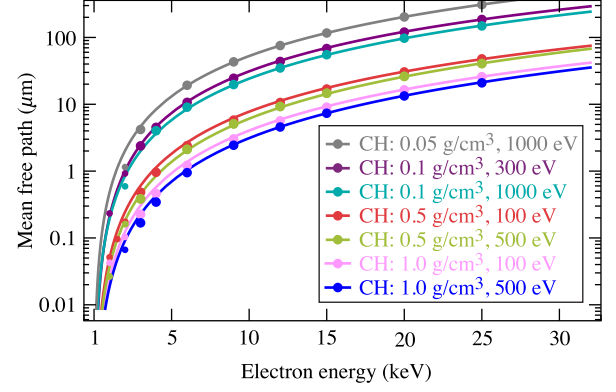


FIG. 4. The nonlocal electron mean free path (MFP) as a function of incoming electron energy. The individual points represent the TD-OF-DFT data shown in Fig. 2, while the solid curves are the corresponding fit for the given plasma conditions and energy. Here, the fitting is a global analytical/numerical model, as shown in Eq. (12).

Then we fit the overall MFP dataset to a single, analytical model with numerically determined coefficients.

Our model is dependent on the plasma temperature $T$, density $\rho$, and initial nonlocal electron kinetic energy $K$. We normalize the plasma parameters ($T$, $\rho$) with values within the conduction zone and use numerically determined coefficients [55]; the coefficients $a_0$, $b_0$, $c_0$, $e_0$, $f_0$, $\alpha$, $\beta$, $\gamma$, $\delta$, $\varepsilon$, $\zeta$, $\omega$, $\phi_{1,2}$, and $\psi_{1,2}$ are given in Table I to four significant figures. In general, the TD-OF-DFT-based model takes the form:

$$\lambda_E = K^2 \left\{ \frac{\langle Z \rangle^2 \, a_0}{4\pi e^4 \, n_e} \left( \frac{K}{\langle Z \rangle} \right)^a \left[ b_0 \left( \frac{T}{400} \right)^\beta \left( \frac{\rho}{0.450} \right)^\gamma \right. \right.$$
$$\left. \left. + c_0 K^\delta \left( \frac{T}{400} \right)^\varepsilon \left( \frac{\rho}{0.450} \right)^\zeta \right] + d_0 \ln (K+1)^\omega \right\}, \quad (12)$$

for $\lambda_E = \lambda_E \, (\rho, T, K)$. The temperature is given in units of eV, and the incoming electron kinetic energy $K$ is given in keV. The mass density $\rho$, electron density $n_e$, elementary charge $e$, and any remaining physical constants are in CGS units. Moreover, the coefficient $d_0$ is dependent on the average ionization state $\langle Z \rangle$ of the background plasma:

$$d_0 = \begin{cases} f_0 \left( \frac{T}{400} \right)^{\phi_1} \left( \frac{\rho}{0.450} \right)^{\psi_1} & \frac{Z_{\max} - \langle Z \rangle}{Z_{\max}} < 0.05 \\ e_0 \left( \frac{T}{400} \right)^{\phi_2} \left( \frac{\rho}{0.450} \right)^{\psi_2} & \text{else}, \end{cases} \quad (13)$$

such that $d_0$ is evaluated one way if $\langle Z \rangle$ falls within 5% of the completely ionized state $Z_{\max} = 3.5$ and another otherwise. We keep the same initial prefactor as the modified Lee-More

TABLE I. Numerically determined coefficients (rounded to four significant figures) for the mean-free-path fitting formula given in Eqs. (12) and (13).

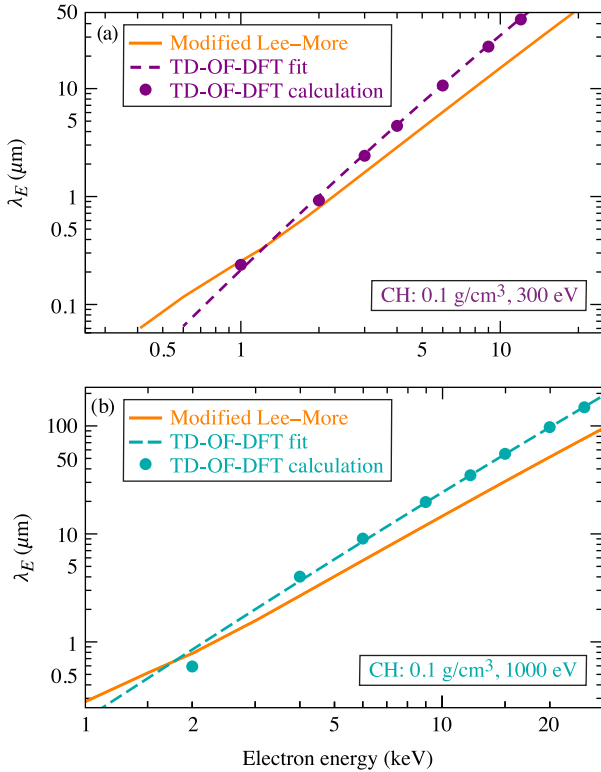| | | | |
|---|---|---|---|
| $a_0 = 2.685 \times 10^{-15}$ | $f_0 = 0.07317$ | $\delta = -0.4074$ | $\phi_1 = -0.6181$ |
| $b_0 = -0.07709$ | $\alpha = 0.3005$ | $\varepsilon = 1.431$ | $\psi_1 = 1.068$ |
| $c_0 = 6.722 \times 10^{-3}$ | $\beta = -0.8279$ | $\zeta = -0.7680$ | $\phi_2 = -1.068$ |
| $e_0 = 0.02740$ | $\gamma = -0.3695$ | $\omega = 0.4547$ | $\psi_2 = -1.162$ |

FIG. 5. CH at either (a) 300 eV or (b) 1000 eV plasma temperature and mass density 0.1 g/cm³. Comparison between the penetration depth $\lambda_E$ given by the modified Lee-More method (orange) to the TD-OF-DFT data (individual points) and corresponding fit (blue and purple curves) obtained by fitting the TD-OF-DFT data and given Eq. (12).

method, shown in Eqs. (4)–(6); the average ionization $\langle Z \rangle = \langle Z(\rho, T) \rangle$ is defined using the first-principles approach introduced in Ref. [56].

Figure 4 shows the global model (solid curves) and the corresponding TD-DFT data (individual points) for each of the seven density-temperature conditions probed. We see the model reaches overall agreement for the higher nonlocal electron energies (5–20 keV), which are closely relevant to the nonlocal transport in LDD conduction-zone conditions. Using this model obtained from our TD-DFT data, we can predict the nonlocal electron MFP for a wide range of plasma conditions relevant to ICF polystyrene plasmas in LDD implosions.

## IV. MODEL COMPARISON

To see the effects of our TD-DFT-based nonlocal electron MFP model on ICF simulations, we compare our results directly to the modified Lee-More method and implement it into the 1D radiation-hydrodynamic code LILAC. The modified Lee-More method, defined by Eqs. (4)–(10), has been used for the past decades in LILAC to predict nonlocal thermal transport. As an illustrative example, our nonlinear model fits of TD-OF-DFT results [Eq. (12)] of $\lambda_E$ are compared with the Lee-More results [Eq. (4)] [12] in Fig. 5 as a function of the nonlocal electron kinetic energy. Figure 5 shows the TD-OF-DFT data (points), the corresponding nonlinear model fit, and
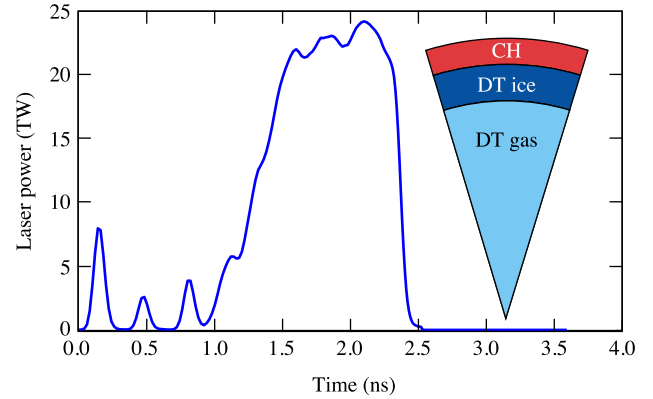


FIG. 6. Laser power as a function of time. Inset: Breakdown of the cryogenic target used in the one-dimensional (1D) hydrodynamic simulation. Deuterium-tritium (DT) gas (380 μm), surrounded by DT ice (50 μm) and escalated by CH (8 μm). The initial mass density of the CH is 1.05 g/cm³. For this paper, we focus on nonlocal stopping in the CH layer.

the modified Lee-More method for a single electron stopped in CH plasma at 0.10 g/cm³ and at temperatures of (a) 300 eV or (b) 1000 eV. Evidently, we see a large difference when we compare our model with the modified Lee-More method; like what we saw in Fig. 3, we note that this difference is a factor of ∼ 2. This indicates that highly energetic electrons (> 5 keV) will penetrate the same CH plasma further than currently predicted, thus carrying more laser energy deeper into the conduction-zone plasma. For low-energy electrons < 5 keV, their MFPs are smaller than what the modified Lee-More predicts. This will evidently change the prediction of laser-target coupling since it is heavily dependent on thermal conduction [14,57], as discussed below.

With the fitted model of TD-OF-DFT results being implemented into LILAC, we can further examine how this new model affects simulations of LDD implosions. Specifically, by comparing LDD target simulations using either our TD-DFT-based model for the nonlocal electron MFP or the traditional modified Lee-More model for nonlocal electron transport, we can identify its effects on the laser-target coupling and the overall implosion dynamics. For our simulations shown in Fig. 6, the target consists of an 8.0-μm-thick CH shell with an initial density $\rho_0 = 1.05$ g/cm³ and outer radius $r = 438$ μm. The layer of DT ice is 50 μm thick with an initial mass density of $\rho_0 = 0.254$ g/cm³, while the capsule is filled with DT gas. The target is shown in Fig. 6, and the inset gives the schematic of the OMEGA scale target. The total laser energy is ∼ 26 kJ, which drives the shell to implode with a maximum velocity of $v_{imp} \sim 400$ km/s. In our simulations, we utilize the nonlocal thermal transport model iSNB [9], for which the electron MFP takes either our TD-OF-DFT-based model or the original modified Lee-More model based upon the material. Moreover, the crossbeam energy transfer (CBET) model [40] for laser energy absorption is invoked. We utilize the first-principles equation of state (EOS) and opacity tables given in Refs. [58–61] to describe the CH and DT target materials.

To understand the effects of MFP models (the TD-OF-DFT-based model developed in this paper vs the modified Lee-More model), we directly compare the density profile and
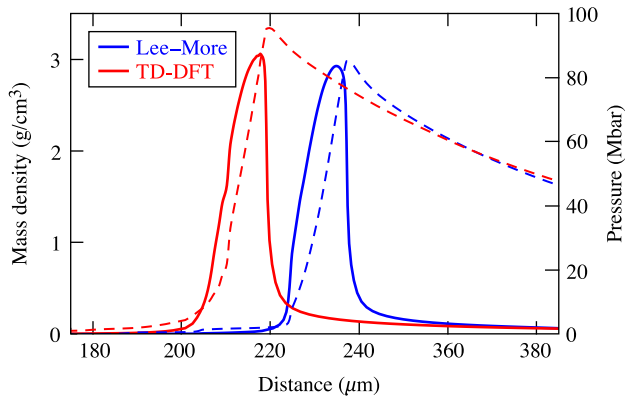
FIG. 7. Comparison at $t = 2.1$ ns between the mass density (left axis, solid lines) and ablation pressure (right axis, dashed lines) using the time-dependent density functional theory (TD-DFT) model (red) and the modified Lee-More model (blue) for the nonlocal electron transport.

ablation pressure at 2.1 ns from the two LILAC simulations in Fig. 7. In Fig. 8, we show the comparison of overall implosion performance. In both Figs. 7 and 8, the red curves represent the LILAC simulation using the TD-OF-DFT-based model, while the blue curves are the LILAC simulations using the standard modified Lee-More model to describe the nonlocal
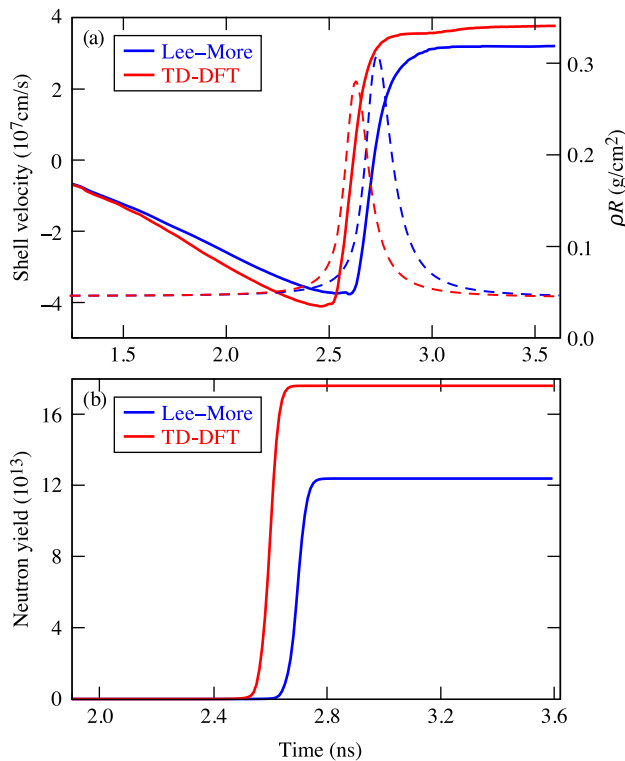


FIG. 8. Comparison of LILAC simulation results using the time-dependent density functional theory (TD-DFT) model (red) and the modified Lee-More model (blue) for nonlocal electron transport. Time evolution of (a) the shell velocity (left axis, solid lines) and compression, $\rho R$ (right axis, dashed lines), and (b) the neutron yield.

electron thermal conduction. In Fig. 7, we observe that the TD-OF-DFT model gives $\sim 12\%$ relative increase in ablation pressure from the standard LILAC simulation, implying the shell has been accelerated further inward. This is consistent with the fact that the TD-OF-DFT model predicts a larger MFP for nonlocal electrons, leading to higher nonlocal thermal conduction. The density profile of the shell is very similar for both simulations; however, the density shell in the standard LILAC simulation peaks at a larger shell radius compared with the one using the modified Lee-More model.

Figure 8(a) shows both the shell velocity (left axis, solid curves) and the compression $\rho R$ (right axis, dashed curves) as a function of time for the two LILAC simulations. We note a clear time shift to earlier bang for our model when compared with the traditional Lee-More model. This is because the TD-DFT predicted MFP of nonlocal electrons is larger than the Lee-More model for projectile electron energies $>3$ keV, as indicated by Fig. 5. Thus, these nonlocal electrons in the TD-DFT model travel further in the conduction-zone CH plasmas and closer to the ablation front, thereby delivering more energy to drive the target with a higher ablation pressure (Fig. 7). Furthermore, as we predict an increase in laser energy penetrating the shell, the target is compressed to its peak areal density earlier than the traditional model, thus causing this leftward shift. Consequently, the imploding shell accelerates faster in TD-DFT-based simulations than the Lee-More case, resulting in a higher implosion velocity [Fig. 8(a)]. That explains the earlier stagnation and bang time in the TD-DFT-based simulation shown in Fig. 8. Using our TD-OF-DFT model for the nonlocal stopping range, we observe $\sim 40\%$ relative increase in the neutron yield from the traditional Lee-More model. In general, we observe significant differences in ICF implosion dynamics when we compare 1D LILAC simulations using our TD-DFT-based model with the current modified Lee-More method for electron stopping range. Radiation-hydrodynamic simulations of ICF implosions are highly integrated, meaning they involve many interconnected physics models. This updated nonlocal thermal conduction model will provide a basis for further calibrating other physics models in the code, such as laser absorption, CBET, EOS, and radiation transport. Aligning these improvements with experiments will be the goal to improve the predictive capabilities of radiation-hydrodynamic codes for reliable ICF target design and simulations.

## V. CONCLUSIONS

In this paper, we devised a global analytical model for the nonlocal electron stopping range in polystyrene plasmas for ICF applications based on TD-OF-DFT calculations. Specifically, our model is applicable for conduction-zone CH plasmas ranging from 0.05 to 1.0 g/cm$^3$ and 100 to 1000 eV. Our TD-OF-DFT results showed lower SP and increased stopping range when compared with analytical models. We implemented this model into the 1D radiation-hydrodynamic code LILAC and performed 1D simulations using a typical OMEGA cryogenic DT target to illustrate its effect on ICF implosions. The results show that the TD-OF-DFT model yielded large differences in terms of implosion dynamics and target performance when compared with the currently implemented nonlocal transport model of the modified

Lee-More stopping range. Our TD-OF-DFT model gives $\sim$ 12% higher ablation pressure due to longer stopping range of nonlocal electrons, which leads to $\sim$ 18% faster implosion and $\sim$ 40% neutron yield than those of the standard LILAC simulation. Reconciling these results with experimental observables, such as trajectory measurements and overall target performance, will require further recalibration of other physics models used in radiation-hydrodynamics codes, such as the CBET model for laser absorption, EOS, and radiation transport. We hope this paper provides the nonlocal thermal transport basis for these recalibration tasks in future studies.

## ACKNOWLEDGMENTS

[1] H. Abu-Shawareb, R. Acree, P. Adams, J. Adams, B. Addis, R. Aden, P. Adrian, B. B. Afeyan, M. Aggleton, L. Aghaian *et al.*, Phys. Rev. Lett. **129**, 075001 (2022).

[2] A. B. Zylstra, O. A. Hurricane, D. A. Callahan, A. L. Kritcher, J. E. Ralph, H. F. Robey, J. S. Ross, C. V. Young, K. L. Baker, D. T. Casey *et al.*, Nature (London) **601**, 542 (2022).

[3] *DOE National Laboratory Makes History by Achieving Fusion Ignition* (Department of Energy, 2023), https://www.energy.gov/articles/doe-national-laboratory-makes-history-achieving-fusion-ignition.

[4] E. M. Campbell, T. C. Sangster, V. N. Goncharov, J. D. Zuegel, S. F. B. Morse, C. Sorce, G. W. Collins, M. S. Wei, R. Betti, S. P. Regan *et al.*, Philos. Trans. R. Soc. A **379**, 20200011 (2021).

[5] R. S. Craxton, K. S. Anderson, T. R. Boehly, V. N. Goncharov, D. R. Harding, J. P. Knauer, R. L. McCrory, P. W. McKenty, D. D. Meyerhofer, J. F. Myatt *et al.*, Phys. Plasmas **22**, 110501 (2015).

[6] S. X. Hu, W. Theobald, P. B. Radha, J. L. Peebles, S. P. Regan, A. Nikroo, M. J. Bonino, D. R. Harding, V. N. Goncharov, N. Petta *et al.*, Phys. Plasmas **25**, 082710 (2018).

[7] E. M. Epperlein and R. W. Short, Phys. Fluids B **3**, 3092 (1991).

[8] G. P. Schurtz, P. D. Nicolaï, and M. Busquet, Phys. Plasmas **7**, 4238 (2000).

[9] D. Cao, G. Moses, and J. Delettrez, Phys. Plasmas **22**, 082308 (2015).

[10] Y. T. Lee and R. M. More, Phys. Fluids **27**, 1273 (1984).

[11] J. Delettrez, R. Epstein, M. C. Richardson, P. A. Jaanimagi, and B. L. Henke, Phys. Rev. A **36**, 3926 (1987).

[12] V. N. Goncharov, O. V. Gotchev, E. Vianello, T. R. Boehly, J. P. Knauer, P. W. McKenty, P. B. Radha, S. P. Regan, T. C. Sangster, S. Skupsky *et al.*, Phys. Plasmas **13**, 012702 (2006).

[13] R. C. Shah *et al.* (unpublished).

[14] R. C. Shah, S. X. Hu, I. V. Igumenshchev, J. Baltazar, D. Cao, C. J. Forrest, V. N. Goncharov, V. Gopalaswamy, D. Patel, F. Philippe *et al.*, Phys. Rev. E **103**, 023201 (2021).

[15] A. B. Zylstra, H. G. Rinderknecht, J. A. Frenje, C. K. Li, and R. D. Petrasso, Phys. Plasmas **26**, 122703 (2019).

[16] L. S. Brown, D. L. Preston, and R. L. Singleton Jr., Phys. Rep. **410**, 237 (2005).

[17] R. L. Singleton Jr., Phys. Plasmas **15**, 056302 (2008).

[18] C. F. Clauser and N. R. Arista, Phys. Rev. E **97**, 023202 (2018).

[19] N. R. Shaffer and S. D. Baalrud, Phys. Plasmas **26**, 032110 (2019).

[20] W. H. Barkas, J. N. Dyer, and H. H. Heckman, Phys. Rev. Lett. **11**, 26 (1963).

[21] M. Peñalba, A. Arnau, and P. M. Echenique, Nucl. Instrum. Methods Phys. Res. B **67**, 66 (1992).

[22] A. J. White, O. Certik, Y. H. Ding, S. X. Hu, and L. A. Collins, Phys. Rev. B **98**, 144302 (2018).

[23] A. D. Baczewski, L. Shulenburger, M. P. Desjarlais, S. B. Hansen, and R. J. Magyar, Phys. Rev. Lett. **116**, 115004 (2016).

[24] K. Jiang and M. Pavanello, Phys. Rev. B **103**, 245102 (2021).

[25] N. M. Gill, C. J. Fontes, and C. E. Starrett, Phys. Rev. E **103**, 043206 (2021).

[26] N. Durante, A. Fortunelli, M. Broyer, and M. Stener, J. Phys. Chem. C **115**, 6277 (2011).

[27] R. J. Magyar, L. Shulenburger, and A. D. Baczewski, Contrib. Plasma Phys. **56**, 459 (2016).

[28] A. J. White, L. A. Collins, K. Nichols, and S. X. Hu, J. Phys.: Condens. Matter **34**, 17 (2022).

[29] A. B. Zylstra, J. A. Frenje, P. E. Grabowski, C. K. Li, G. W. Collins, P. Fitzsimmons, S. Glenzer, F. Graziani, S. B. Hansen, S. X. Hu *et al.*, Phys. Rev. Lett. **114**, 215002 (2015).

[30] Y. H. Ding, A. J. White, S. X. Hu, O. Certik, and L. A. Collins, Phys. Rev. Lett. **121**, 145001 (2018).

[31] S. Malko, W. Cayzac, V. Ospina-Bohórquez, K. Bhutwala, M. Bailly-Grandvaux, C. McGuffey, R. Fedosejevs, X. Vaisseau, An. Tauschwitz, J. I. Apiñaniz *et al.*, Nat. Commun. **13**, 2893 (2022).

[32] E. Runge and E. K. U. Gross, Phys. Rev. Lett. **52**, 997 (1984).

[33] N. D. Mermin, Phys. Rev. **137**, A1441 (1965).

[34] W. Kohn and L. J. Sham, Phys. Rev. **140**, A1133 (1965).

[35] T. Sjostrom and J. Daligault, Phys. Rev. B **88**, 195103 (2013).

[36] R. P. Feynman, N. Metropolis, and E. Teller, Phys. Rev. **75**, 1561 (1949).

[37] A. J. White and L. A. Collins, Phys. Rev. Lett. **125**, 055002 (2020).

[38] B. Shpiro, M. D. Fabian, E. Rabani, and R. Baer, J. Chem. Theory Comput. **18**, 1458 (2022).

[39] Y. Cytter, E. Rabani, D. Neuhauser, and R. Baer, Phys. Rev. B **97**, 115207 (2018).

[40] M. F. Hutchinson, Commun. Stat. Simul. Comput. **18**, 1059 (2007).

[41] M. D. Feit, J. J. A. Fleck, and A. Steiger, J. Comput. Phys. **47**, 412 (1982).

[42] J. P. Perdew, K. Burke, and M. Ernzerhof, Phys. Rev. Lett. **77**, 3865 (1996).

[43] S. Lehtola, C. Steigemann, M. J. T. Oliveira, and M. A. L. Marques, SoftwareX **7**, 1 (2018).

[44] S. Goedecker, M. Teter, and J. Hutter, Phys. Rev. B **54**, 1703 (1996).

[45] C. Hartwigsen, S. Goedecker, and J. Hutter, Phys. Rev. B **58**, 3641 (1998).

[46] M. Krack, Theor. Chem. Acc. **114**, 145 (2005).

[47] S. Zhang, V. V. Karasiev, N. Shaffer, D. I. Mihaylov, K. Nichols, R. Paul, R. M. N. Goshadze, M. Ghosh, J. Hinz, R. Epstein *et al.*, Phys. Rev. E **106**, 045207 (2022).

[48] R. Car and M. Parrinello, Phys. Rev. Lett. **55**, 2471 (1985).

[49] J. S. Tse, Annu. Rev. Phys. Chem. **53**, 249 (2002).

[50] L. A. Collins, S. R. Bickham, J. D. Kress, S. Mazevet, T. J. Lenosky, N. J. Troullier, and W. Windl, Phys. Rev. B **63**, 184110 (2001).

[51] A. Mazarro, P. M. Echenique, and R. H. Ritchie, Phys. Rev. B **27**, 4117 (1983).

[52] P. Sigmund and A. Schinner, J. Appl. Phys. **128**, 100903 (2020).

[53] S. P. Ahlen, Rev. Mod. Phys. **52**, 121 (1980).

[54] L. H. Andersen, P. Hvelplund, H. Knudsen, S. P. Möller, J. O. P. Pedersen, E. Uggerhöj, K. Elsener, and E. Morenzoni, Phys. Rev. Lett. **62**, 1731 (1989).

[55] S. Smit, in MultiNonlinearModelFit (Wolfram Research, 2022), https://resources.wolframcloud.com/FunctionRepository/resources/MultiNonlinearModelFit.

[56] S. X. Hu, L. A. Collins, V. N. Goncharov, J. D. Kress, R. L. McCrory, and S. Skupsky, Phys. Plasmas **23**, 042704 (2016).

[57] S. X. Hu, D. T. Michel, A. K. Davis, R. Betti, P. B. Radha, E. M. Campbell, D. H. Froula, and C. Stoeckl, Phys. Plasmas **23**, 102701 (2016).

[58] S. X. Hu, B. Militzer, V. N. Goncharov, and S. Skupsky, Phys. Rev. Lett. **104**, 235003 (2010).

[59] S. X. Hu, L. A. Collins, J. P. Colgan, V. N. Goncharov, and D. P. Kilcrease, Phys. Rev. B **96**, 144203 (2017).

[60] S. X. Hu, B. Militzer, V. N. Goncharov, and S. Skupsky, Phys. Rev. B **84**, 224109 (2011).

[61] S. X. Hu, L. A. Collins, V. N. Goncharov, J. D. Kress, R. L. McCrory, and S. Skupsky, Phys. Rev. E **92**, 043104 (2015).